Türkiye Jeoloji Bülteni
Geological Bulletin of Turkey
69 (2026) 103-120
doi:10.25288/tjb.1767998

Estimation of Basement Relief in the Isparta Basin by Applying Spectral Filtering and Local Optimisation-Based Inversion Techniques to Gravity Data

Gravite Verilerine Spektral Filtreleme ve Lokal Optimizasyon-Tabanlı Ters Çözüm Teknikleri Uygulayarak Isparta Baseninde Temel Kaya Topografyasının Tahmini

Rezzan Pekcan Ekinci[1,*], Çağlayan Balkaya[2]

[1] *Muş Alparslan University, Program of Emergency and Disaster Management, Muş, Türkiye*
[2] *Süleyman Demirel University, Department of Geophysical Engineering, Isparta, Türkiye*

• Geliş/Received: 18.08.2025 • Düzeltilmiş Metin Geliş/Revised Manuscript Received: 20.10.2025 • Kabul/Accepted: 23.10.2025
• Çevrimiçi Yayın/Available online: 04.01.2026 • Baskı/Printed: 31.01.2026
Araştırma Makalesi/Research Article *Türkiye Jeol. Bül. / Geol. Bull. Turkey*

Abstract: The Isparta Basin is a tectonically complex depression situated at the junction between the Western Anatolian extensional province and the Tauride orogenic belt. It lies near the intersection of the Hellenic and Cyprus arcs, forming the Isparta Angle. This transitional zone is characterised by intense crustal deformation, complex fault systems, and active seismicity, making it a key area for geophysical investigation. Microgravity anomalies were analysed to assess the thickness of the basin's sedimentary deposits. A 2-D Fourier transformation-based procedure was used to decompose the gravity data into regional and residual components. This spectral filtering step isolated shallow subsurface signals from broader tectonic influences, thereby providing a robust foundation for depth modelling by enhancing the resolution of near-surface features that are often masked by deeper structural trends. Residual gravity anomalies were further examined using both 2-D and 3-D local optimisation-based inversion techniques. These complementary methods allowed for cross-validation of results mathematically and improved confidence in the derived structural interpretations. The resulting basement depth estimates demonstrate consistency and align well with the established geological framework of the Isparta Basin, including known fault geometries and stratigraphic boundaries, with the inversion results indicating maximum sedimentary fill thickness of approximately 0.53 km. This result has practical implications for disaster management, particularly in assessing the potential for seismic amplification. Thick sedimentary sequences can substantially affect ground-motion characteristics during earthquakes, especially within basin environments. Therefore, mapping the spatial distribution of sedimentary accumulation contributes to more informed regional risk assessments and supports the development of targeted mitigation strategies. These findings are expected to provide valuable input for land-use planning and infrastructure resilience in the Isparta Basin, offering essential baseline information for authorities and engineers involved in seismic hazard mitigation.

Keywords: Basement relief, inversion, Isparta basin, microgravity, spectral filtering.

Öz: *Isparta Havzası, Batı Anadolu genişleme bölgesi ile Toros orojenik kuşağının birleşim noktasında yer alan tektonik olarak karmaşık bir çöküntü alanıdır. Helen ve Kıbrıs yaylarının kesişimine yakın konumuyla Isparta Açısını oluşturmaktadır. Bu geçiş zonu, yoğun kabuksal deformasyon, karmaşık fay sistemleri ve aktif sismisite ile karakterize edilmekte olup, jeofiziksel araştırmalar açısından önemli bir çalışma sahasıdır. Bu kendine özgü tektonik ortamda sedimanter dolgu kalınlığını belirlemek amacıyla mikrogravite anomalileri analiz edilmiştir. Gravite verileri, 2-B Fourier dönüşümüne dayalı bir yöntem kullanılarak bölgesel ve rezidüel bileşenlerine ayrıştırılmıştır. Bu spektral filtreleme aşaması, yüzeye yakın sinyalleri daha geniş tektonik etkilerden etkin bir şekilde ayırarak, genellikle daha*

Correspondence / *Yazışma*: r.ekinci@alparslan.edu.tr

derin yapılar tarafından maskelenen sığ özelliklerin çözünürlüğünü artırmış ve derinlik modellemesi için sağlam bir temel oluşturmuştur. Rezidüel gravite anomalileri, hem 2-B hem de 3-B lokal optimizasyon-tabanlı ters çözüm teknikleriyle incelenmiştir. Bu tamamlayıcı yöntemler, sonuçların matematiksel olarak doğrulanmasına olanak tanımış ve elde edilen yapısal yorumların güvenilirliğini arttırmıştır. Elde edilen temel kaya derinliği tahminleri, Isparta Havzası'nın bilinen jeolojik yapısıyla, özellikle fay geometrileri ve stratigrafik sınırlarla uyum göstermektedir ve ters çözüm sonuçları maksimum sedimanter dolgu kalınlığının yaklaşık 0,53 km olduğunu göstermektedir. Tahmin edilen sedimanter dolgu kalınlığı, afet yönetimi açısından pratik önem taşımaktadır. Özellikle havza ortamlarında, kalın sedimanter birikimler deprem sırasında yer hareketi özelliklerini önemli ölçüde etkileyebilir. Bu nedenle, sedimanter birikimin uzamsal dağılımının haritalandırılması, daha bilinçli bölgesel risk değerlendirmelerine katkıda bulunmakta ve hedefli azaltma stratejilerinin geliştirilmesini desteklemektedir. Bu bulguların, Isparta Havzası'nda arazi kullanım planlaması ve altyapı dayanıklılığı için değerli çıktılar oluşturacağı ve sismik tehlike azaltma çalışmalarına katılan yetkililer ve mühendisler için temel bilgi kaynağı sağlayacağı öngörülmektedir.

Anahtar Kelimeler: *Isparta baseni, mikrogravite, spektral filtreleme, temel kaya topografyası, ters çözüm.*

INTRODUCTION

Sedimentary basins are the primary continental settings where prolonged subsidence creates depressional terrains at lower altitudes than the surrounding regional uplands, facilitating the accumulation of sedimentary deposits (Onajite, 2014; Weismann et al., 2015). Sedimentary basins evolve through subsidence and sedimentation driven by a variety of tectonic processes. In extensional regimes, crustal stretching forms grabens that accommodate rapid clastic infill, whereas flexural loading adjacent to growing orogens induces broad, regional down-warping and basin development (Allen and Allen, 2005). Thermal subsidence occurs due to lithospheric cooling and isostatic readjustment. This process increases accommodation space and promotes gradual thickening of the sedimentary sequence over geological time (Allen and Allen, 2005). The composition of basin fills provides a record of key aspects of palaeoenvironments. Fluvial, lacustrine, deltaic and shallow-marine depositional systems deliver sediments of varying grain size and mineralogy, generating complex, multi-storey stratigraphy that archive palaeogeographic evolution and climatic shifts (Catuneanu, 2006). Subsequent deformation (e.g. faulting, folding or compaction) of these sequences preserves a chronicle of tectonic pulses and structural maturation (Allen and Allen, 2005). Global sea-level fluctuations exert decisive control on sedimentation patterns. Marine transgressions inundate continental shelves with siliciclastic and carbonate deposits, while regressions concentrate terrigenous influx (Catuneanu, 2006). Distinct basin types (e.g. continental rifts, passive margins, intra-cratonic sag basins) display characteristic fill architectures. Rift basins commonly exhibit rapid, asymmetric sedimentation, whereas passive margins develop extensive, gently dipping clastic wedges. Such architectural differences reflect the interplay of subsidence rate, sediment supply and basin geometry (Catuneanu, 2006). Sedimentary fills also form vital groundwater reservoirs (Hunt et al., 2022). Porous and fractured sedimentary formations comprise major aquifer systems supplying irrigation and potable water, especially in arid and semi-arid zones where surface water is limited. Aquifer yield and water quality are governed by the depositional and diagenetic characteristics of the basin fill (Todd and Mays, 2004). The geothermal energy potential of sedimentary sequences has attracted increasing interest. Thick, high-heat-flux basins may yield hot water or steam for district heating and power generation, with reservoir performance dependent on porosity, permeability and thermal conductivity of the fill (Wu et al., 2025).

In seismically active regions, basin geometry and fill properties intensely influence ground-motion characteristics. The natural resonance frequency of a sedimentary basin depends on sediment thickness and shear-wave velocity. This can lead to significant seismic-wave amplification and increased damage to overlying structures (Borcherdt, 1970). Variations in a sedimentary basin's geometry and internal architecture can markedly influence seismic wave amplification and transmission, which result in differences in ground shaking intensity and distinct propagation patterns (Ghose et al., 2023). Moreover, water-saturated, low-density sediment layers elevate liquefaction potential during strong ground-motions, a factor critical to seismic design and risk mitigation (Seed and Idriss, 1982). Integrating seismic studies with complementary microgravity surveys enhances characterisation of basin architecture and fault networks beneath sedimentary layers (Pamuk et al., 2017; Büyüksaraç et al., 2023, Bektaş et al., 2025). This integration improves the accuracy of ground-motion modelling and underpins more effective disaster-risk-reduction strategies in tectonically active basins.

Despite the critical importance of accurately characterising sedimentary deposit thickness for urban seismic hazard assessment, an inadequate number of studies have been conducted to quantify sedimentary fill thickness beneath the city in the Isparta Basin. In addition, the Isparta Basin has remained largely underexplored in terms of gravity-based inversion studies. In contrast, most geophysical research has concentrated on the western Anatolian extensional regime, particularly the Büyük Menderes and Gediz grabens within the Aegean Graben System, which have attracted considerable attention due to their pronounced tectonic activity and well-defined subsurface geometries (e.g. Sari and Şalk, 2006; Işık and Şener, 2009; Lima and Silva, 2014; Timur et al., 2019; Ekinci et al., 2021, 2023; Roy et al., 2025). This study aims to fill that gap by providing new insights into the basin's subsurface configuration and the sedimentary architecture of the Isparta region, with a specific focus on the densely populated and seismically active urban area. The 2-D Fourier-based anomaly separation technique was applied to microgravity anomalies to isolate residual signals tied to shallow subsurface structures. These residual anomalies were then inverted using both 2-D and 3-D approaches. By integrating these methodologies, we produced reasonable estimates of basement relief depth, which provide sedimentary fill thickness in the Isparta Basin.

STUDY AREA and DATA

Tectonic and Geological Setting of the Isparta Basin

Türkiye is located at the convergence zone of several major tectonic plates, namely the African, Arabian, and Eurasian plates (Figure 1). This geodynamic interaction gives rise to a highly active tectonic regime that governs much of the deformation across the Anatolian plate (McKenzie, 1972; Bozkurt, 2001). Western Anatolia is shaped by extensional tectonics due to westward movement of the Anatolian plate, which escapes the collision between the Arabian and Eurasian plates through strike-slip and normal faulting (Şengör and Yılmaz, 1981; Reilinger et al., 2006). Within this broader tectonic framework, two significant subduction-related arc systems play critical roles: the Hellenic (Crete) Arc to the southwest and the Cyprus Arc to the south (Figure 1). Both arcs represent subduction zones where the African plate is descending beneath the Eurasian margin (Barka and Reilinger, 1997). These arcs not only accommodate plate convergence but also influence crustal deformation, seismicity, and magmatism across the eastern Mediterranean region (Barka and Reilinger, 1997; Robertson et al., 2003).

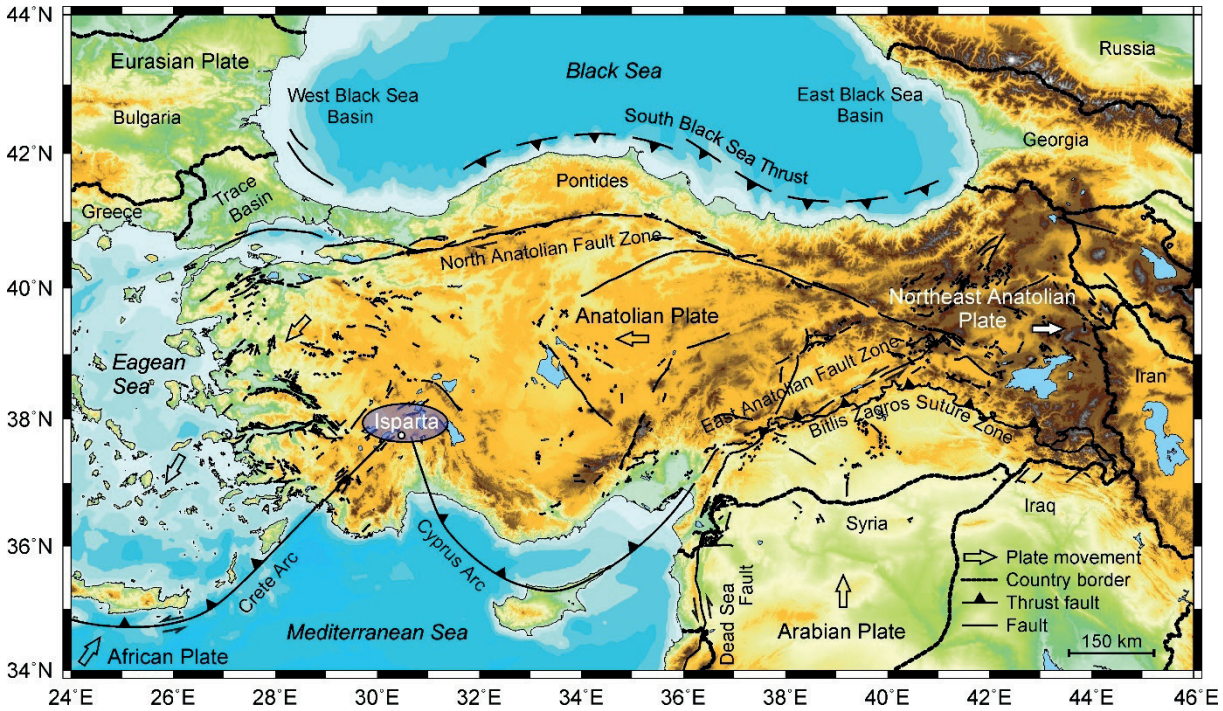

Figure 1. Simplified neotectonic map of Türkiye (compiled from Okay & Tüysüz 1999; Yiğitbaş *et al.* 2004; Ekinci & Yiğitbaş, 2012, 2015; Ekinci *et al.* 2013, 2020). GMT software (Wessel & Smith 1995) was used to produce the map.

Şekil 1. *Türkiye'nin basitleştirilmiş neotektonik haritası (Okay & Tüysüz, 1999; Yiğitbaş¸et al., 2004; Ekinci ve Yiğitbaş, 2012, 2015; Ekinci vd., 2013 ve 2020'den derlenmiştir). Haritayı üretmek için GMT yazılımı (Wessel ve Smith, 1995) kullanılmıştır.*

At the intersection of these two arcs lies a geologically intricate area known as the Isparta Angle, which marks a transition between compressional and extensional tectonic domains. This structurally unique zone is shaped by the interplay of arcuate fault systems and varying stress regimes, and it serves as a key area to understand the tectonic evolution of southwestern Anatolia (Şengör and Yılmaz, 1981). The Isparta Basin is located at the apex of this angle, acting as a structurally controlled sedimentary depression influenced by both local and regional tectonic forces. There is consensus that the Isparta Angle attained its present position during the neotectonic period. Based on paleomagnetic data, Kissel and Poisson (1986) and Piper et al. (2002) suggest that the Beydağları carbonate massif forming the western limb of the Isparta Angle may have experienced counterclockwise rotation throughout the Miocene.

The basin is delineated by two prominent fault systems: the Fethiye-Burdur Fault Zone trending northwest along its western margin, and the Akşehir Fault Zone trending northeast on its eastern flank. These fault systems converge in the north with the Sultandağı Fault, outlining a triangular tectonic setting (Koçyiğit and Özacar, 2003). The structural geometry of the basin promotes localised subsidence and accumulation of thick sedimentary sequences. Seismological data confirm that these faults are seismically active, with multiple moderate-to-large earthquakes occurring over the past century (Taymaz and Price, 1992; Wright et al., 1999; Emre et al., 2003). The Isparta region also contains local-scale structures,

such as the Davraz and Kayı Faults, which further influence the seismic behaviour within the basin. Instrumental earthquake recordings show clusters of microseismicity near the urban centre and surrounding areas. These patterns correlate with local fault lines, which indicate ongoing deformation even within the sedimentary basin interior (Koçyiğit and Özacar, 2003).

Isparta Basin has a diverse stratigraphy consisting of sedimentary, volcanic, and volcaniclastic units from the Mesozoic to the Quaternary. The stratigraphic succession in the study area is grouped into autochthonous and allochthonous units (Şenel, 2007a & b; Demer, 2008). The autochthonous sequence comprises the Menteşe Formation (Msm), Davras Limestone (Msd), Söbüdağ Limestone (Krüds, member of Davras Limestone), Çiğdemtepe Limestone (Krüç), Koçtepe Formation (Tk), Kayıköy Formation (Ti), and Gölcük Volcanics (pyroclastics as PQgp and volcanic lavas as PQgv), all of which are unconformably overlain by slope debris (Qy) and alluvial fan deposits (Figure 2). The allochthonous assemblage consists of the Gökçebağ Complex (Mg) and the Akdağ Limestone (Ma). The Menteşe Formation consists of grey to greyish-black, medium- to thick-bedded, densely vuggy dolomitic limestones that form the basal unit of the Davras Limestone and contain abundant megalodontid moulds (Demer, 2008). The Davras Limestone has extensive outcrops in the eastern part of the study area. The unit is dated to the Upper Triassic Turonian (Görmüş and Özkul, 1995). The Söbüdağ Limestone constitutes the Late Cretaceous carbonate section of the Davras Limestone (Demer, 2008). The rudist-bearing carbonates of the Late Cretaceous Çiğdemtepe Formation unconformably overlie the Davras Limestone unit (Karaman et al., 1988; Yıldız and Toker, 1991). Based on its lithological and faunal characteristics, the unit is interpreted to have been deposited in a shallow lagoonal setting, with locally restricted lagoonal conditions (Görmüş and Özkul, 1995). The Çiğdemtepe Limestone is represented by pelagic limestones and is predominantly composed of light-cream to whitish-grey, platy pelagic limestone (Demer, 2008). Based on its faunal and lithological characteristics, the unit is interpreted to have been deposited in a pelagic environment (Karaman et al., 1988; Görmüş and Özkul, 1995). The Koçtepe Formation begins with a conglomeratic-breccia basal layer and this is succeeded by thin- to medium-bedded pelagic marls that range in colour from red and reddish-pink to wine-red, locally exhibiting kidney-shaped weathering (Yalçınkaya, 1989). The flysch-character Kayıköy Formation comprises interbedded claystone, siltstone, sandstone, and conglomerate. The dominant lithologies are claystone and sandstone (Karaman et al., 1988; Görmüş and Özkul, 1995). The pyroclastics largely consist of weakly consolidated interbedded tuff, tuffite, and pumice layers (Demer, 2008). Volcanic lavas occur as subvolcanic stocks and dikes composed of trachyandesite and trachyte, and these volcanic stocks are locally overlain by pyroclastic deposits derived from the Gölcük volcano (Demer, 2008). Slope debris typically developed in front of steep slopes where high hills descend into the plain. They consist of clay, silt, sand, gravel, and blocks (Demer, 2008). The alluvial fan deposits provide the most extensive outcrops in the study area. Within the plain, the deposit consists of unconsolidated sand, gravel, clay, and silt-sized materials, with grains predominantly composed of limestone, chert, tuff, and volcanic clasts (Demer, 2008). The Gökçedağ Complex comprises basic to ultrabasic lithologies containing blocks of variable size. It exhibits a multi-coloured appearance, predominantly green, and locally displays olistostromal features (Yalçınkaya, 1989). The Akdağ Limestone, which overlies the rock units in the study area together with ophiolitic mélanges, comprises white, medium- to thick-bedded recrystallised limestones whose bedding is completely disrupted, and which are highly fractured and jointed (Demer, 2008).

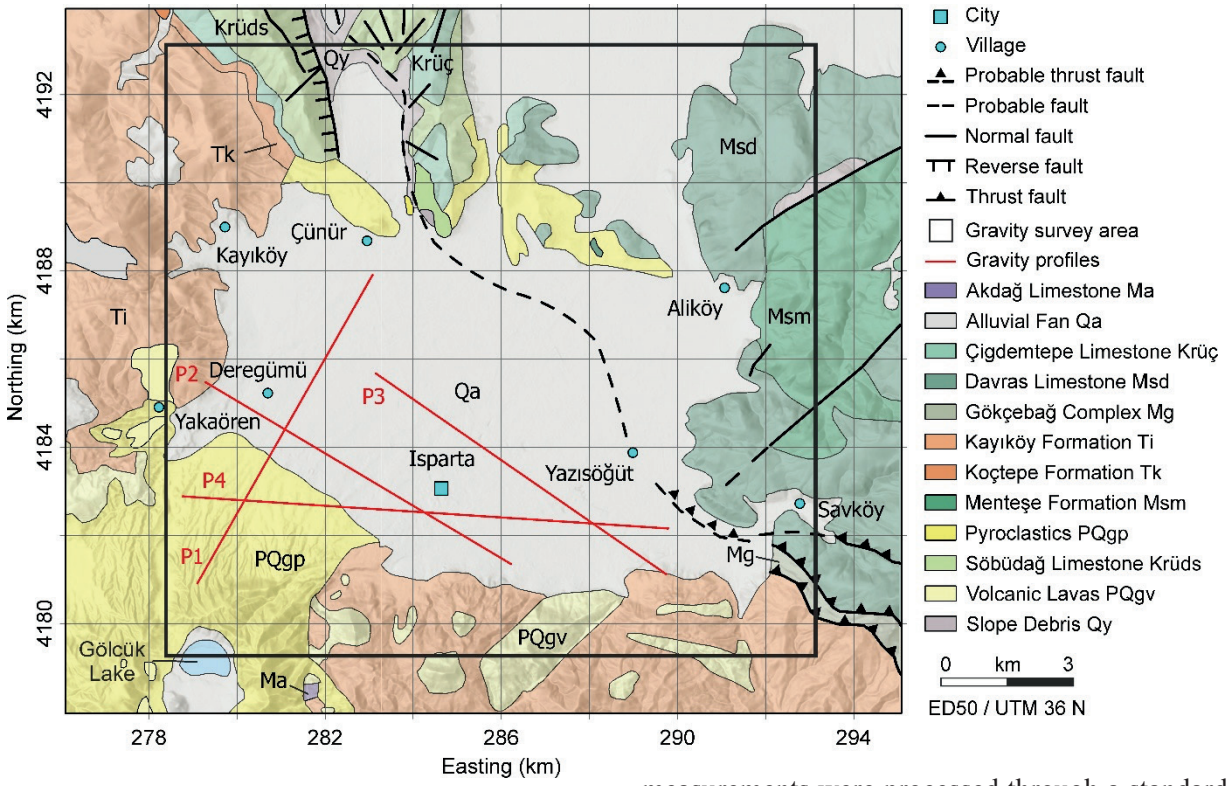

Figure 2. Geologic map of Isparta Basin (compiled from Şenel, 2007a & b; Demer, 2008).

Şekil 2. *Isparta Baseninin jeoloji haritası (Şenel, 2007a ve b ve Demer, 2008'den derlenmiştir).*

Microgravity data

The microgravity data were acquired using a CG-5 Scintrex gravimeter, which provides high-precision measurements and includes internal correction systems for temperature, tilt, and tidal effects (Beyhan et al., 2017; Silahtar et al., 2020). A total of 108 gravity stations were measured across an area approximately 14 km south to north and 14.8 km west to east (Beyhan et al., 2017). While the survey targeted a gridded layout, practical constraints such as terrain and road access led to minor deviations from the planned grid (Silahtar et al., 2020). To control for instrumental drift, a fixed base station was established, and readings were taken at regular two-hour intervals throughout the survey. After fieldwork, the raw gravity measurements were processed through a standard sequence of corrections to isolate the geological signal from external influences (Beyhan et al., 2017; Silahtar et al., 2020). These corrections included instrumental drift adjustments, tidal corrections, latitude corrections, and free-air corrections. The last step was the Bouguer correction, which modelled the gravitational effect of the rock mass between the station and sea level, using a reduction density of 2.4 g/cm³ based on regional rock properties (Dolmaz, 2007). The data set used here was digitised from Beyhan et al. (2017).

METHODOLOGY

Regional and Residual Separation via 2-D Fourier Transform

To separate the microgravity anomalies into regional and residual components, a 2-D Fourier-based spectral filtering method was applied. This method decomposes gravity anomalies into their

components to distinguish shallow from deep crustal effects. It identifies regional and residual contributions in the wave-number domain. The microgravity data set *G(x,y)*, was transformed into the wave number domain via fast Fourier transform (FFT), and its spectral representation was calculated using the following equation (Buttkus, 2000).

$$\hat{G}(k_x,k_y)=\sum_{x=0}^{N_x-1}\sum_{y=0}^{N_y-1}G(x,y)\,.\,e^{\left(-2\pi i\left(\frac{k_x x}{N_x}+\frac{k_y y}{N_y}\right)\right)} \quad (1)$$

In this equation, N_x and N_y represent the number of samples (or data points) in the x and y directions of the microgravity data grid, respectively. In Fourier space, the energy density of each component is defined by the following equation.

$$E(k_x,k_y)=\left|\hat{G}(k_x,k_y)\right|^2 \quad (2)$$

These energy values were grouped at specific intervals based on the magnitude of the radial wavelength, as given below (Blakely, 1996).

$$r_{k_x,k_y}=\sqrt{{k_x}^2+{k_y}^2} \quad (3)$$

Thus, the resulting 1-D energy spectrum was calculated, and the average energy values for each radial wavelength band were obtained via the following equation.

$$E(r)=\left(\frac{1}{N_r}\right)\sum_{r_{k_x,k_y}\in[r,r+\Delta r)}\left|\hat{G}(k_x,k_y)\right|^2 \quad (4)$$

The first derivative of the spectral energy curve, $\partial E/\partial r$, indicates the variation in energy distribution. At the point of the steepest negative derivative on this curve, the abrupt drop in energy density is identified as the critical threshold radius, R_{opt}. This value is used as an optimal threshold in the wave number domain to separate regional and residual components. With this approach, instead of selecting a fixed threshold, the separation is performed based on the data-specific spectral behaviour, which allows for effective isolation of shallow anomalies in the microgravity data. The obtained spectrum is separated into regional and residual components according to this threshold value, using the equations given below (Buttkus, 2000).

$$\hat{G}_{rej}(k_x,k_y)=\hat{G}(k_x,k_y)\,.\,\mathbb{1}\left[r_{k_x,k_y}\le R_{opt}\right] \quad (5)$$

$$\hat{G}_{rez}(k_x,k_y)=\hat{G}(k_x,k_y)\,.\,\mathbb{1}\left[r_{k_x,k_y}> R_{opt}\right] \quad (6)$$

Through this process, a masking operation was applied, followed by an inverse Fourier transform to transition into the spatial domain. Both components were then obtained in the spatial domain using the following expressions.

$$G_{rej}(x,y)=F^{-1}\left[\hat{G}_{rej}(k_x,k_y)\right]=\frac{1}{N_xN_y}\sum_{k_x=-\frac{N_x}{2}}^{\frac{N_x}{2}-1}\sum_{k_y=-\frac{N_y}{2}}^{\frac{N_y}{2}-1}\hat{G}_{rej}(k_x,k_y)\,.\,e^{\left(2\pi i\left(\frac{k_x x}{N_x}+\frac{k_y y}{N_y}\right)\right)} \quad (7)$$

$$G_{rez}(x,y)=F^{-1}\left[\hat{G}_{rez}(k_x,k_y)\right]=\frac{1}{N_xN_y}\sum_{k_x=-\frac{N_x}{2}}^{\frac{N_x}{2}-1}\sum_{k_y=-\frac{N_y}{2}}^{\frac{N_y}{2}-1}\hat{G}_{rez}(k_x,k_y)\,.\,e^{\left(2\pi i\left(\frac{k_x x}{N_x}+\frac{k_y y}{N_y}\right)\right)} \quad (8)$$

2-D inversion of gravity anomalies

The gravity anomaly at any point caused by 2-D rectangular blocks is expressed by the following equation (Rao and Murty, 1978).

$$\Delta g(k)=\sum_{i=2}^{N-1}[F_k(z)]_{ZT(i)} \quad (9)$$

Here, $\Delta g(k)$ is the observed gravity anomaly at point x_k, $F_k(z)$ is the gravity effect of the block located below station *i*, *ZT(i)* is the depth to the top of the block below *i*. The derivation with respect to the depth parameter is given below.

$$\frac{\partial F_{k(z)}}{\partial z}=-2G\Delta\rho\left[\arctan\left(\frac{x_k+\frac{dx}{2}}{z}\right)-\arctan\left(\frac{x_k-\frac{dx}{2}}{z}\right)\right] \quad (10)$$

Here *G,* is the gravitational constant, $\Delta\rho$ is the density contrast and *dx* denotes the station interval. The normal equations are given as follows (Murty and Rao, 1989).

$$\sum_{i=1}^{N}\left(\sum_{k=1}^{M}\left(\frac{\partial\Delta g(k)}{\partial a_i}\right)\left(\frac{\partial\Delta g(k)}{\partial a_j}\right)+\lambda\delta_{ij}\right)\Delta a_i=\sum_{k=1}^{M}\Delta g(k)\left(\frac{\partial\Delta g(k)}{\partial a_j}\right),\ j=1,2,\dots,N \quad (11)$$

Here $\Delta g(k)$, is the misfit at the kth data point Δa_i, represents the parameter update, $\left(\frac{\partial \Delta g(k)}{\partial a_i}\right)$ is the partial derivative of the misfit with respect to the ith parameter, δ_{ij} denotes the Kronecker delta, λ is the damping factor, N is the number of the parameters and M represents the number of observations. According to this inversion scheme, the algorithm begins with the Marquardt damping factor set to $\lambda = 0$, corresponding to a diagonal coefficient multiplier of $(1 + \lambda) = 1.0$ in the normal equations. This means that the first iteration proceeds with a standard Gauss-Newton step. If the objective function does not improve, the damping factor is adaptively increased using the control parameter NLAMDA, which serves as an iteration index for adjusting λ. The relationship between these variables is given by this equation.

$$\lambda = \frac{1}{2}\,(2^{\,\mathrm{NLAMDA}-1} - 1), \tag{12}$$

This results in successive λ values (0.5, 1.5, 3.5, etc). When convergence is achieved, NLAMDA is reduced and λ returns to zero. The iteration terminates when λ becomes excessively large (typically greater than 15.0), or when the objective function reaches the predefined tolerance. To provide a normalised measure of data fit, we used the root mean square error (RMSE), calculated after each iteration, as follows.

$$\mathrm{RMSE} = \sqrt{\frac{1}{N}\sum_{i=2}^{N-1}[g_{\mathrm{obs}}(x_i) - g_{\mathrm{cal}}(x_i)]^2} \tag{13}$$

Here, $g_{obs}(x_i)$ and $g_{cal}(x_i)$ represent the observed and calculated gravity anomalies at station i, respectively, and N denotes the total number of observation points. In this formulation, the first and last observation points are excluded because they correspond to artificially extended boundary nodes added for numerical stability at the profile ends. The details of the inversion algorithm are given in Murty and Rao (1989).

3-D inversion of gravity anomalies

The method presented by Rao et al. (1990) focuses on the 3-D inversion of gravity anomalies caused by subsurface geological structures, modelled as a juxtaposition of rectangular prisms. We used a constant density contrast between the sedimentary fill and the underlying basement. The forward modelling step computes the vertical gravity anomaly at a surface point caused by such a prism. The exact expression of the anomaly is derived by integrating Newton's law over the volume of the prism. For a single prism, the expression is given below (Rao et al., 1990).

$$\Delta g(x,y) = G\Delta\rho\left[Z_2B_1 - Z_1B_2 + \frac{X_2}{2}B_3 + \frac{X_1}{2}B_4 + \frac{Y_2}{2}B_5 + \frac{Y_1}{2}B_6\right] \tag{14}$$

Here G, is the gravitational constant, X_1, X_2 and Y_1, Y_2 are the horizontal offsets from the prism centre to its edges in the x-and y-directions, respectively. B_1 to B_6 are composite terms involving arctangent and logarithmic functions of the distances from the observation point to the corners (vertices) of the prism as given in Rao et al. (1990). To invert the gravity data, the depth to the base of each prism is estimated such that the calculated anomalies match the observed ones. The procedure begins with an initial depth estimate based on a linear approximation of the Bouguer slab formula, adapted from Bott's method as given below

$$Z(x,y) = \frac{\Delta g_{obs}(x,y)}{2\pi G\rho} \tag{15}$$

This provides a rough starting model for the basement interface. Following this, the inversion proceeds iteratively. At each iteration, the gravity anomaly is calculated by summing the contributions from all prisms. The discrepancy between the observed and calculated values is then used to update the basement depth (Rao et al., 1990).

$$Z^{new}(x,y) = Z^{old}(x,y) + \frac{\Delta g_{obs}(x,y) - \Delta g_{cal}(x,y)}{2\pi G\rho} \quad (16)$$

The iterative correction continues until residual anomalies fall below a set tolerance or the iteration limit is reached. We used the same RMSE function given previously, serving as a diagnostic measure of convergence. The process yields a 3-D basement relief model that explains the gravity data under constant density contrast. This method is particularly well suited for modelling basin structures where lateral density variations are negligible. It offers a practical compromise between interpretational accuracy and computational efficiency. The details of the inversion algorithm are given in Rao et al. (1990).

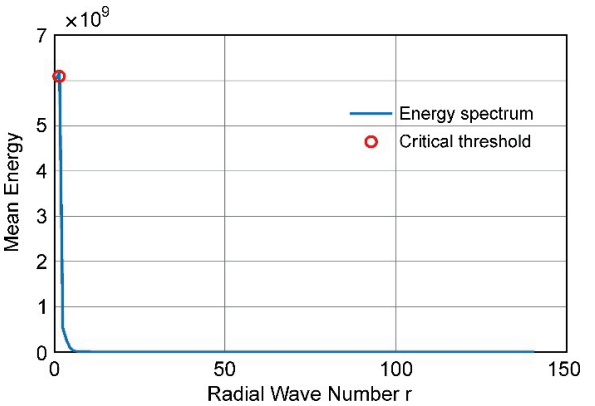

Figure 3. Spectral energy distribution and critical threshold radius.

Şekil 3*. Spektral enerji dağılımı ve belirlenen kritik eşik yarıçapı.*

ANALYSES and FINDINGS

In the applications, the critical threshold radius R_{opt} was determined as 1 (Figure 3). This value represents a very small circular region in the spectral domain, located very close to the origin, which includes only the components with the longest wavelengths. Mathematically, this implies that only the components with a radius value of at most one are classified as regional, while the rest are included in the residual component. In this case, the regional component becomes highly simplified, and shallow structures located at shorter wavelengths become more pronounced in the residual component. The threshold value of 1 is not a ratio or percentage, but rather a unit of radial distance defined in wave number space, which is related to the data dimensions according to the definition of the Fourier transform. Such low threshold values can enable clearer observation of the residual signal, especially in regions where crustal trends are weak and local anomalies are dominant.

Figure 4 presents a sequential analysis of the Bouguer gravity data through spectral decomposition. Figure 4a shows the complete Bouguer gravity anomaly, reflecting the combined effects of both deep and shallow density variations. The regional component obtained via 2-D Fourier transform, highlighting long-wavelength features that likely correspond to deeper crustal structures or broader isostatic trends, is shown in Figure 4b. The residual component, which isolates short-wavelength anomalies associated with shallow subsurface features such as sedimentary fill variations and fault-controlled basement relief is shown in Figure 4c. When compared with the geological map in Figure 2, a notable spatial correlation emerges between the residual gravity anomalies and the mapped sedimentary-volcaniclastic sequences in the central Isparta Basin. Areas of relatively negative residual anomaly values coincide with the known extent of thick sedimentary and volcaniclastic deposits, while positive anomalies generally correspond to the outcropping or shallowly buried basement units. This spatial agreement confirms that the residual gravity component effectively captures geologically meaningful variations in subsurface

density and validates the use of spectral filtering techniques in this context. The coherence between residual anomaly patterns and surface geology supports the reliability of the applied procedures. This consistency indicates that the gravity-based interpretations are geologically sound.

Here, we used a density contrast of -0.58 g/cm^3 (Silahtar et al., 2020) in the 2-D and 3-D inversion procedures. The 2-D inversion results obtained from four gravity profiles are shown in Figure 5. Figure 6 illustrates the convergence behaviour of the 2-D inversion algorithm, shown here for the P4 profile since the inversions performed for the other profile data sets exhibited nearly identical convergence characteristics. The outcomes reveal a consistent pattern of sedimentary deposit thickness and basement topography across the Isparta Basin. The sedimentary fill reaches a maximum thickness of approximately 0.52 km, indicating significant accommodation space within the basin interior.

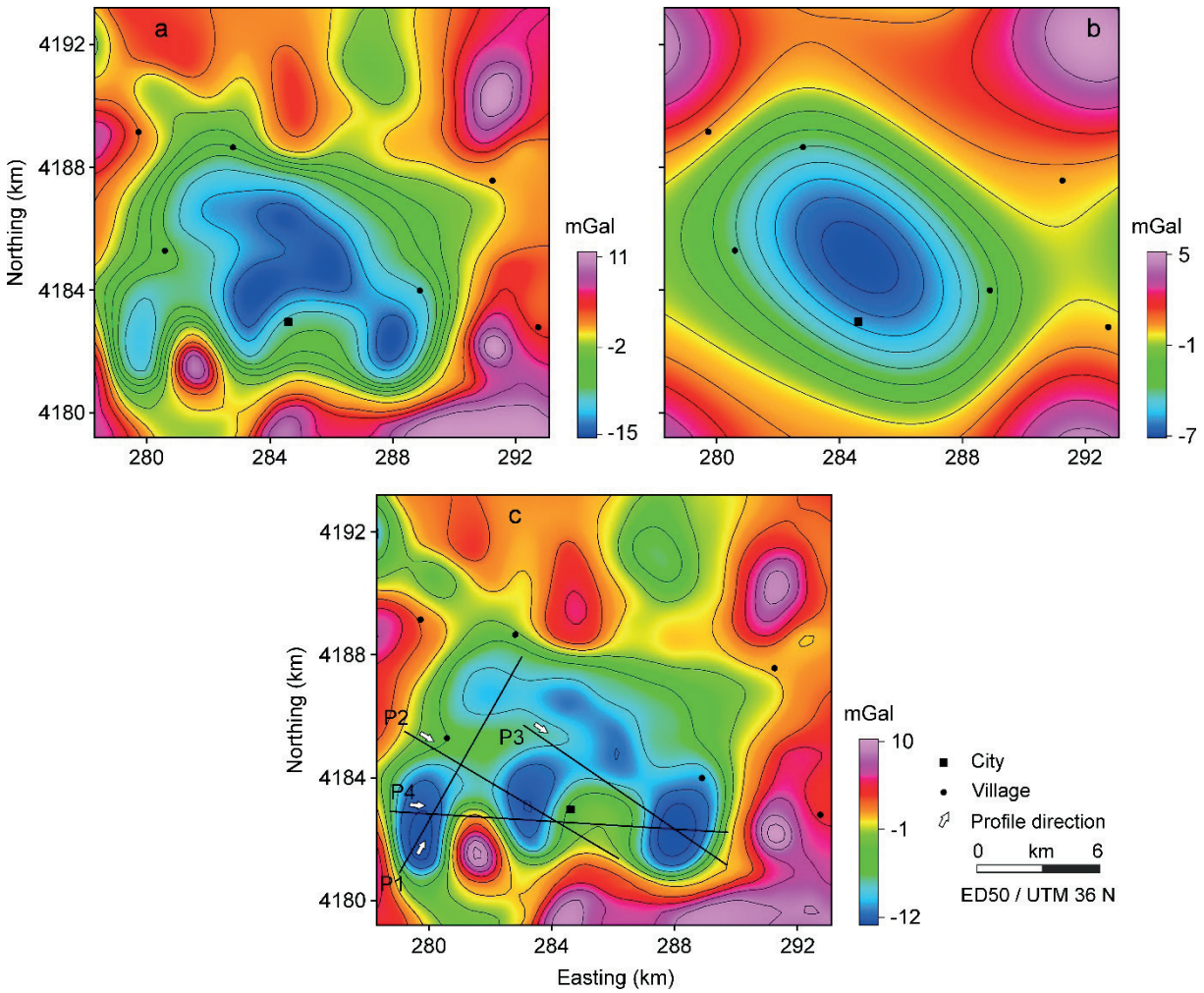

Figure 4. a) Bouguer gravity anomaly, **(b)** regional anomaly and **(c)** residual anomaly for the Isparta Basin. The profiles used for 2-D inversion are shown in **(c)**. Black square and dots show settlements given in Figure 2.

Şekil 4. a) *Isparta Baseni Bouguer gravite anomalisi,* ***(b)*** *bölgesel anomali ve* ***(c)*** *rezidüel anomali. 2-B ters çözüm için kullanılan profiler* ***(c)*** *de verilmiştir. Siyah kare ve noktalar Şekil 2'de verilen yerleşim yerlerini göstermektedir.*

The basement surface exhibits an undulatory (wavy) morphology characterised by alternating highs and lows, which suggest a tectonically controlled structural configuration rather than a purely depositional subsidence pattern. This undulation likely results from block faulting mechanisms associated with extensional tectonics, as well as superimposed deformation due to compressional reactivation. The structural irregularity is consistent across all profiles, which highlights a high degree of internal coherence and strengthens the reliability of the inversion results. The geological map of the Isparta Basin (Figure 2) supports these interpretations. The basin is bounded by major fault zones such as the Fethiye-Burdur Fault Zone and the Akşehir Fault Zone, which converge in the north to define a triangular tectonic depression. These active fault systems, along with smaller-scale faults like the Davraz and Kayı Faults, likely contribute to the observed relief of the basement. Furthermore, the presence of unconsolidated Quaternary alluvial fans, slope debris, and volcaniclastic sequences in the central part of the basin corresponds spatially with areas of maximum accumulation inferred from gravity inversion. The abrupt basement depth changes at short lateral distances may reflect fault-controlled subsidence zones or tilted fault blocks, supporting the interpretation of a tectonically segmented basement structure.

Geologically, the Isparta Basin lies within a complex transition zone between the compressional Tauride belt and the extensional Western Anatolian domain. The undulatory basement relief observed in this study likely reflects these dual tectonic influences. The basement highs may correspond to relatively uplifted blocks of Mesozoic carbonates (e.g., Davras Limestone), while the lows align with graben-like structures infilled by younger Neogene-Quaternary clastic sediments and volcanics. This interpretation is consistent with the mapped stratigraphy, where older autochthonous carbonate and flysch sequences are unconformably overlain by thick basin-fill deposits.

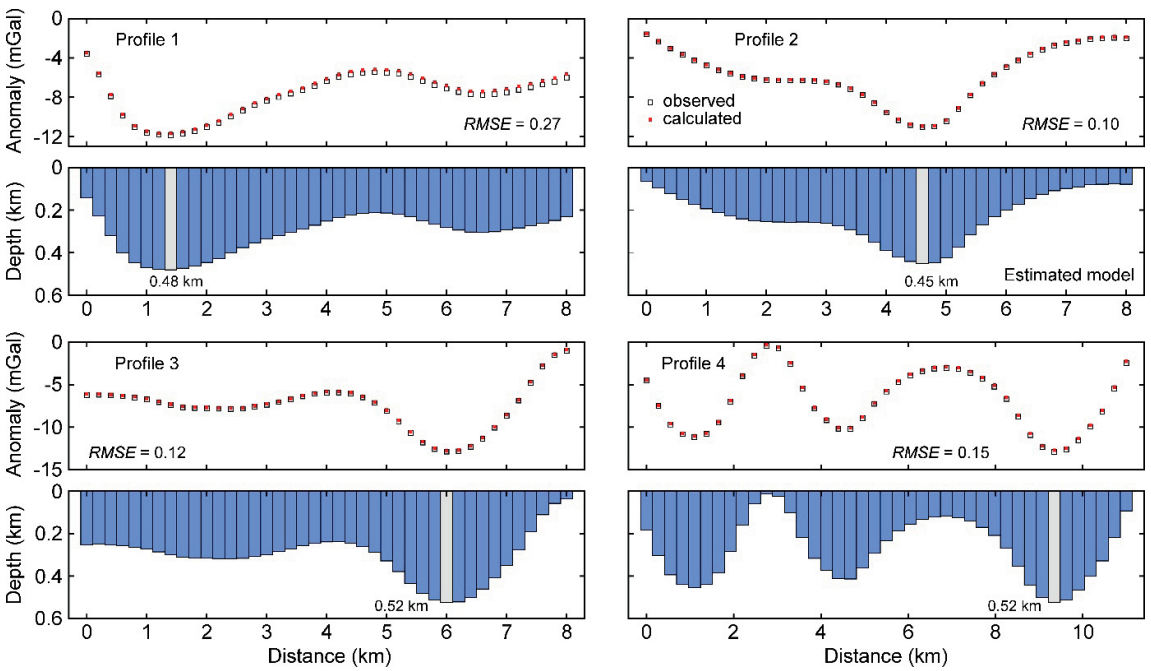

Figure 5. 2-D inversion results of selected four profiles.

Şekil 5*. Seçilen dört profile ait 2-B ters çözüm sonuçları.*

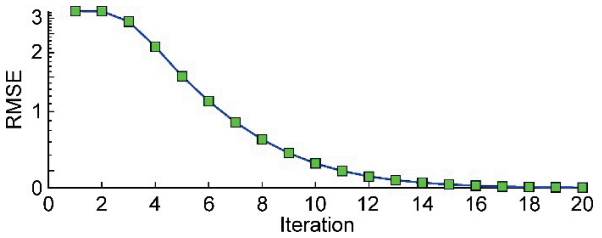

Figure 6. Convergence behaviour of the 2-D inversion algorithm.

Şekil 6*. 2-B ters çözüm algoritmasının yakınsama davranışı.*

The 3-D inversion results presented in Figure 7a illustrate the detailed spatial distribution of basement topography across the Isparta Basin, with the sedimentary fill thickness effectively visualized as the vertical distance between the modelled basement and the surface. The model reveals that the thickest sedimentary accumulations (>0.5 km) occur predominantly in the central and southwestern parts of the basin, forming an arcuate zone that aligns well with the mapped extents of alluvial fan deposits and volcaniclastic units shown on the geological map (Figure 2). This sedimentary wedge appears to taper toward the northeast and southeastern flanks of the basin, where basement highs are more prominent and shallow carbonate rocks (e.g., Davras and Çiğdemtepe Limestones) crop out or lie close to the surface. The deposit thickness pattern suggests structurally controlled deposits, possibly bounded and shaped by major fault systems such as the Fethiye-Burdur Fault Zone to the west and the Akşehir Fault Zone to the east. The observed asymmetry in sedimentary fill distribution may reflect tilted fault blocks or syn-depositional subsidence linked to extensional tectonics.

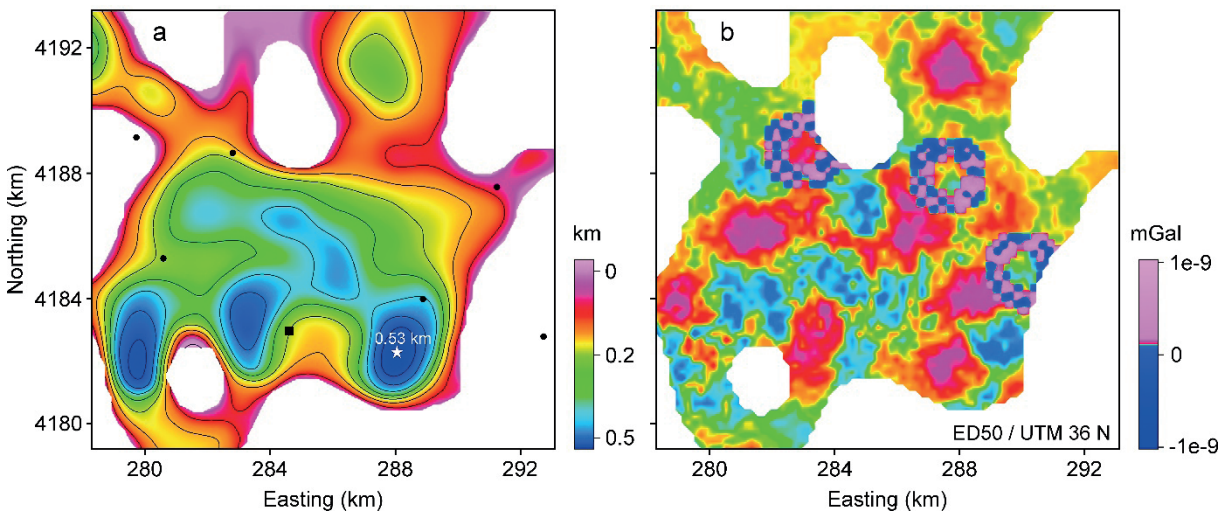

Figure 7. a) The basement depth obtained from 3-D inversion and **(b)** the difference between observed and calculated anomalies. Black square and dots show settlements given in Figure 2.

Şekil 7*. **a)** 3-B ters çözüm ile elde edilen temel kaya derinliği **(a)** ve **(b)** ölçülen ile hesaplanan anomali arasındaki fark. Siyah kare ve noktalar Şekil 2'de verilen yerleşim yerlerini göstermektedir.*

The inversion algorithm excluded positive gravity anomalies to avoid contamination from high-density basement outcrops or volcanic intrusions. Because sedimentary deposits are less dense than the basement rocks, they generate negative gravity anomalies. Therefore, to ensure the 3-D inversion accurately represents the sedimentary thickness distribution, only these negative anomalies were used. This exclusion led to localised blank zones in the deposit thickness map, particularly over areas dominated by high-density lithologies. Despite this, the calculated infill distribution closely corresponds with the 2-D inversion results, indicating high internal consistency across different inversion methodologies. The misfit map (Figure 7b) further supports the reliability of the 3-D inversion, showing minimal discrepancy between the observed and calculated gravity anomalies. Thus, the forward model adequately captures the basin's subsurface density structure. These findings, when considered alongside the regional tectonic framework of the Isparta Angle, where compressional and extensional regimes converge, emphasise the complex interplay between basin infill patterns and active fault systems. The agreement between geophysical models and geological observations supports the validity of the inversion methodologies and confirms that the resulting sedimentary fill thickness distribution is both geologically plausible and geophysically robust. Figure 8 presents the variation of RMSE values with iteration number for the 3-D inversion. A clear convergence trend is observed, which indicates that the optimisation process effectively minimised the misfit between the observed and calculated gravity data. In addition, to explicitly assess the internal consistency between the 2-D and 3-D inversions, the P4 profile was extracted from the 3-D basement model along the same trace used for the 2-D inversion (Figure 9). The 3-D-derived P4 section closely repeats the 2-D solution (Figure 6), including the position of basement highs and lows and the peak sedimentary thickness within the central part of the basin. Very minor discrepancies are confined to the margins and are attributable to methodological differences between the two schemes, rather than substantive mismatch. This cross-sectional agreement corroborates the strong 2-D/3-D coherence and provides additional confidence in the basin-scale interpretations presented here.

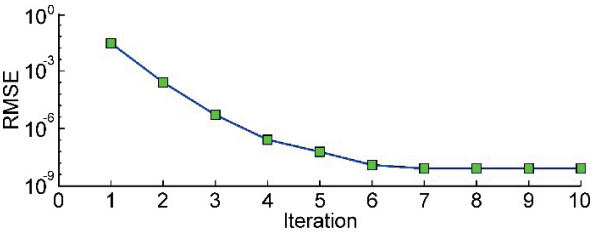

Figure 8. Convergence behaviour of the 3-D inversion algorithm.

Şekil 8*. 3-B ters çözüm algoritmasının yakınsama davranışı.*

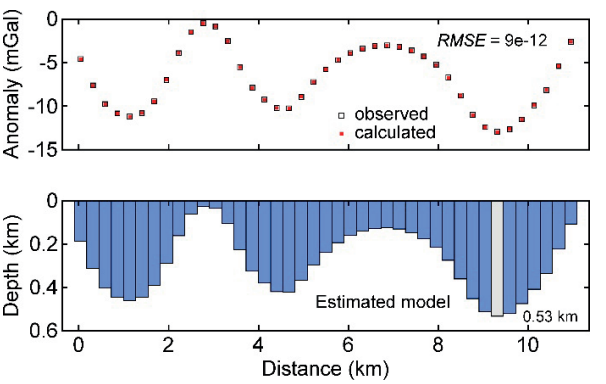

Figure 9. P4 profile extracted from 3-D inversion results.

Şekil 9*. 3-B ters çözüm sonuçlarından elde edilen P4 profili.*

The spatial variability of sediment thickness revealed by the gravity inversion provides fundamental insights into the local dynamic behaviour of the Isparta Basin. This information is

particularly relevant for seismic microzonation and urban planning, as variations in sediment thickness directly control site response parameters such as fundamental resonance frequency, amplification potential, and the impedance contrast between the sedimentary package and underlying bedrock. Areas characterised by thicker sedimentary accumulations are expected to have lower resonance frequencies and stronger amplification of long-period ground-motions, while shallower zones tend to respond at higher frequencies. These relationships enable the gravity-derived sediment thickness model to serve as a first-order dataset for delineating microzonation zones and guiding future site-specific investigations, including shear-wave velocity profiling and ambient noise analyses. Therefore, the proposed approach offers a cost-effective and regionally consistent framework for identifying areas with distinct dynamic characteristics, which can support engineering design, seismic hazard assessment, and disaster-risk mitigation strategies within the Isparta Basin.

CONCLUSIONS

The application of a 2-D Fourier-based spectral filtering method, followed by both 2-D and 3-D local optimisation-based inversions, produced a reasonable model of the Isparta Basin's basement relief and sedimentary fill. By selecting a data-specific threshold radius in the wave number domain, shallow residual anomalies, those most directly tied to sedimentary fill thickness and fault-controlled relief, were successfully isolated from deeper regional trends. Geologically, the Isparta Basin occupies the apex of the Isparta Angle, where the extensional regime of Western Anatolia converges with the compressional Tauride orogen and intersects the Hellenic and Cyprus subduction arcs. Its stratigraphy spans Mesozoic carbonates and flysch through Neogene-Quaternary volcanics and clastics, all unconformably overlain by thick alluvial-fan and slope-debris deposits. Two principal fault systems, the northwest-trending Fethiye-Burdur Fault Zone and the northeast-trending Akşehir Fault Zone, frame the basin and drive block-faulted subsidence. These structures are mirrored in the gravity anomalies: long-wavelength regional trends trace deep crustal flexure and subduction-related loading, while short-wavelength residual anomalies sharply define block-faulted basement highs and sedimentary fills. Residual anomalies highlight zones where sedimentary accumulations reach up to 0.53 km. The undulatory basement topography, marked by alternating uplifted highs and subsiding lows spaced roughly 2-5 km apart, closely follows the trace of the Fethiye-Burdur and Akşehir Fault segments. The highs coincide with outcropping Mesozoic carbonates, whereas the deepest lows align with thick Neogene-Quaternary clastic and volcaniclastic infill. This pattern implies that block-fault rotations and differential subsidence have shaped the basin architecture. Moreover, the amplitude of the residual gravity signal scales with the density contrast between rigid carbonate blocks and softer sedimentary fills, strengthening the idea that gravity anomalies faithfully map both structural and depositional features. These patterns indicate a history of episodic extensional faulting driven by the westward escape of the Anatolian block. Localised compressional reactivation at fault intersections produced the wavy basement relief and variable sedimentary thickness in the Isparta Basin. 2-D inversion along four profiles revealed an undulating basement surface with highs corresponding to uplifted Mesozoic limestone blocks and lows marking Neogene-Quaternary graben-infills. The 3-D inversion further delineated an arcuate deposit in the central and southwestern basin where sedimentary fills exceed 0.5 km in thickness, tapering toward basement highs in the northeast and southeast. The strong agreement between the 2-D and 3-D inversion models, further confirmed by the P4

profile extracted from the 3-D basement surface (Figure 9), and their close correspondence with both residual gravity patterns and mapped geology, collectively attest to the robustness and reliability of the integrated workflow applied to the Isparta Basin. This consistency across different inversion dimensions strengthens the credibility of the derived basement relief and sediment thickness distributions, enhancing confidence in the overall geological interpretation of the basin.

From a seismic-hazard perspective, the mapped sedimentary thickness and fault-controlled undulations are crucial. They strongly influence ground-motion amplification, basin resonance, and liquefaction risk in the densely populated central part of the Isparta Basin. The combined spectral-filtering and inversion approaches for gravity data therefore provide essential data for seismic microzonation and targeted land-use planning, offering a practical framework for identifying zones with differing site-response characteristics and for designing resilient infrastructure throughout the Isparta Basin within this dynamic extensional-compressional transition zone.

GENİŞLETİLMİŞ ÖZET

Bu çalışmada, Isparta Havzası'nın jeodinamik evrimine bağlı olarak gelişen havza içindeki sedimanter dolgu kalınlığını ile temel kaya üst yüzeyinin uzaysal değişimini belirlemek amacıyla mikrogravite anomalileri, 2-B Fourier dönüşümü tabanlı spektral filtreleme ve 2-B ile 3-B ters çözüm algoritmalarının kullanımına dayanan bir metodolojiyle analiz edilmiştir. İlk aşamada gravite verisi, dalga sayısı uzayında veri odaklı bir kritik eşik yarıçapı belirlenerek bölgesel eğilimler ile sığ yapı sinyalleri birbirinden ayrılmış, derin kabuksal eğilimi temsil ettiği düşünülen uzun dalga boylu bileşenlerle yerel blok-fay kontrollü anomaliler izole edilmiştir. Bu yaklaşım, dalga sayısı uzayında tanımlanan kritik yarıçapının yalnızca uzun dalga boylu bileşenleri bölgesel eğilim olarak kabul edilmesine dayanmaktadır ve böylece zayıf kabuksal eğilimlerin etkisinde, sığ anomalilerin daha net biçimde ayırt edilmesi sağlanmıştır. Ardından rezidüel anomaliler üzerinde dört ayrı 2-B profil ve tüm çalışma alanını kapsayan 3-B modelleme adımları gerçekleştirilmiş, iteratif güncellemelerle hem gözlenen hem de hesaplanan gravite anomalileri arasındaki çakışmazlık ölçütü minimize edilerek yaklaşık 0,53 km'lik maksimum sedimanter dolgu kalınlığı ve blok-fay segmentasyonu sonucunda oluşmuş dalgalı bir temel kaya topoğrafyası elde edilmiştir. Jeolojik olarak havza, Batı Anadolu'nun genişleme rejimi ile Toros kuşağının sıkışma etkilerinin kesiştiği, Hellen ve Kıbrıs alt dalma zonlarının yakınında yer alan "Isparta Açısı" içinde konumlanmış ve Mezozoik karbonatları ile Neojen-Kuaterner volkanoklastik ve klastik birimleri, kalın alüvyon yelpazeleri ve yamaç molozlarıyla üst üste gelmiştir. Kuzeybatı-güneydoğu doğrultulu Fethiye-Burdur ve kuzeydoğu-güneybatı yönlendirmeli Akşehir Fay Zonu, havzanın iki ana sınırını oluşturarak blok-fay kontrollü yükselme ve çöküntü alanlarının şekillenmesine neden olmuş, bu yapısal kontrol spektral ayrıştırma sonrasında elde edilen rezidüel anomalilerde negatif anomalilerin kalın sedimanter birikimiyle, pozitif anomalilerin ise sığ karbonat ve ofiyolitik bloklarla örtüşmesiyle doğrulandığı düşünülmüştür. Elde edilen dalgalı temel kaya yüzeyi, 2-5 km ölçeğinde birbirini izleyen yükseltiler ve çukurluklar formunda ortaya çıkmış, bu özellik Anadolu plakasının batıya kaçışıyla tetiklenen faylanma aşamalarının, lokal olarak sıkışmaya uğrayan segmentlerde yeniden etkinleşme göstergesi olarak yorumlanmıştır. Hem 2-B hem de 3-B çözümler arasında sağlanan yüksek uyumluluk ile gravite anomalileri arasındaki tutarlı korelasyon, spektral filtreleme ve lokal optimizasyon yöntemlerinin jeolojik ve jeofiziksel verilerle güçlü bir örtüşme sergilediğini kanıtlamıştır.

Uygulama açısından, haritalanan maksimum 0,53 km civarındaki sedimanter dolgu kalınlıkları, depreme duyarlı mikrobölgeleme çalışmalarına kritik girdi sağlamaktadır ve rezonans frekansına ve yer hareketi büyütme potansiyeline bağlı olarak zemin tepki davranışının ve sıvılaşma riskinin değerlendirilmesinde doğrudan kullanılabilecek derinlik profilleri sunmaktadır. Sedimanter dolgu kalınlığındaki uzaysal değişim, yerel zemin tepkisi ve dolgu-temel kaya empedans kontrastı hakkında birinci dereceden bilgi sağlayarak mühendislik tasarımı, kentsel planlama ve afet risk azaltımı süreçlerine ön bilgi oluşturur. Ayrıca, blok-fay kontrolündeki kalın birikimlerin konumu, kritik altyapı tesislerinin ve yoğun nüfus alanlarının güvenli bölgelerde konumlandırılması için arazi kullanımı planlamasında rehber olma potansiyeline sahiptir. Sonuç olarak, kullanılan veri işleme aşamaları, Isparta Havzası gibi dinamik bir genişleme-sıkışma geçiş zonunda hem bölgesel tektonik segmentasyonu hem de yerel çökelme alanlarının yeraltı yapısını ortaya koymuştur. Böylece gravite verisinin, jeotektonik yorumlardan mühendislik ve afet yönetimi uygulamalarına kadar geniş bir yelpazede temel ön bilgi kaynağı olarak kullanılabileceği gösterilmiştir.

ACKNOWLEDGEMENTS

We gratefully acknowledge Can Ertekin for his technical expertise in digitising the Bouguer gravity anomaly map and compiling the geological map. We also sincerely thank the three anonymous reviewers for their constructive comments and valuable suggestions, which greatly helped to improve the clarity, quality, and overall presentation of the manuscript. This paper forms part of the PhD dissertation conducted by the corresponding author (RPE) at the Graduate School of Natural and Applied Sciences, Süleyman Demirel University, under the supervision of the co-author (ÇB).

ORCID

Rezzan Pekcan Ekinci https://orcid.org/0000-0002-5367-8857
Çağlayan Balkaya https://orcid.org/0000-0002-0191-8564

REFERENCES

Allen, P. A. & Allen, J. R. (2005). *Basin analysis: principles and applications*. 2nd edition. Blackwell, Oxford, 549 pp.

Barka, A. & Reilinger, R. (1997). Active tectonics of the Eastern Mediterranean region: deduced from GPS, neotectonic and seismicity data. *Annals of Geophysics*, *40*(3), 587–610. https://doi.org/10.4401/ag-3892

Bektaş, Ö., Büyüksaraç, A., Sarıtepe, H. E., Önal, K. M., Canbaz, O., Eyisüren, O., Pamuk, E., Akın, Ö., Akar, F. & Koşaroğlu, S. (2025). Shear-wave velocity model of the Sivas City (inner eastern, Türkiye) using Rayleigh wave ellipticity inversion controlled by 2D microgravity modeling. *Acta Geophysica*, 1-19. https://doi.org/10.1007/s11600-025-01682-7

Beyhan, G., Kanbur, M.Z., Selim H.H., Utkucu, M., Silahtar, A. & Budakoğlu, E. (2017). *Isparta havza yapısının jeofizik yöntemler ile modellenmesi ve senaryo deprem sismik tehlike haritalarının hazırlanması* (Proje No: 114Y836). Project Report, TÜBİTAK.

Blakely, R.J. (1996). *Potential theory in gravity and magnetic applications*. Cambridge University press.

Borcherdt, R.D. (1970). Effects of local geology on ground motion near San Francisco Bay. *Bulletin of the Seismological Society of America*, *60*, 29–61. https://doi.org/10.1785/BSSA0600010029

Bozkurt, E. (2001). Neotectonics of Turkey - a synthesis. *Geodinamica Acta*, *14*(1–3), 3–30. https://doi.org/10.1016/S0985-3111(01)01066-X

Buttkus, B. (2000). *Spectral Analysis and Filter Theory in Applied Geophysics*. Springer, Berlin, Heidelberg.

Büyüksaraç, A., Eyisüren, O., Bektaş, Ö. & Karaca, Ö. (2023). Bedrock depth calculation of Çanakkale (Turkey) basin using Rayleigh ellipticity and microgravity survey. *Geofísica Internacional*, *62*, 387–401. https://doi.org/10.22201/igeof.2954436xe.2023.62.1.1447

Catuneanu, O. (2006). *Principles of Sequence Stratigraphy*. Elsevier, Amsterdam, 375 pp.

Demer, S.A. (2008). *Isparta ve yakın çevresi yeraltısularının hidrojeolojik, hidrojeokimyasal ve izotop jeokimyasal incelenmesi ve içme suyu kalitesinin izlenmesi* [PhD Thesis]. Süleyman Demirel Üniversitesi.

Dolmaz, M. N. (2007). An aspect of the subsurface structure of the Burdur-Isparta area, SW Anatolia, based on gravity and aeromagnetic data, and some tectonic implications. *Earth, Planets and Space*, *59*, 5–12. https://doi.org/10.1186/BF03352016

Ekinci, Y. L. & Yiğitbaş, E. (2012). Geophysical approach to the igneous rocks in the Biga Peninsula (NW Turkey) based on airborne magnetic anomalies: geological implications. *Geodinamica Acta, 25*, 267–285. https://doi.org/10.1080/09853111.2013.858945

Ekinci, Y.L., Ertekin, C. & Yiğitbaş, E. (2013). On the effectiveness of directional derivative based filters on gravity anomalies for source edge approximation: synthetic simulations and a case study from the Aegean Graben System (Western Anatolia, Turkey). *Journal of Geophysics and Engineering, 10*(3), Article 035005. https://doi.org/10.1088/1742-2132/10/3/035005

Ekinci, Y. L. & Yiğitbaş, E. (2015). Interpretation of gravity anomalies to delineate some structural features of Biga and Gelibolu peninsulas, and their surroundings (north–west Turkey). *Geodinamica Acta, 27*, 300–319. https://doi.org/10.1080/09853111.2015.1046354

Ekinci, Y. L., Büyüksaraç, A., Bektaş, Ö. & Ertekin, C. (2020). Geophysical investigation of Mount Nemrut Stratovolcano (Bitlis, Eastern Turkey) through aeromagnetic anomaly analyses. *Pure and Applied Geophysics, 172*, 3243–3264. https://doi.org/10.1007/s00024-020-02432-0

Ekinci, Y. L., Balkaya, Ç., Göktürkler, G. & Ai, H. (2023). 3-D gravity inversion for the basement relief reconstruction through modified success-history-based adaptive differential evolution. *Geophysical Journal International*, *235*(1), 377–400. https://doi.org/10.1093/gji/ggad222

Ekinci, Y. L., Balkaya, Ç., Göktürkler, G. & Özyalın, Ş. (2021). Gravity data inversion for the basement relief delineation through global optimization: a case study from the Aegean Graben System, western Anatolia, Turkey. *Geophysical Journal International*, *224*(2), 923–944. https://doi.org/10.1093/gji/ggaa492

Emre, O., Duman, T. Y., Doğan, A., Özalp, S., Tokay, F. & Kuşçu, I. (2003). Surface faulting associated with the Sultandağı earthquake (Mw 6.5) of 3 February 2002, Southwestern Turkey. *Seismological Research Letters*, *74*(4), 382–392. https://doi.org/10.1785/gssrl.74.4.382

Ghose, R., Persaud, P. & Clayton, R.W. (2023). Basin structure for earthquake ground motion estimates in urban Los Angeles mapped with nodal receiver functions. *Geosciences*, *13*, 320. https://doi.org/10.3390/geosciences13110320

Görmüş, M. & Özkul, M. (1995). Gönen-Atabey (Isparta) ve Ağlasun (Burdur) Arasındaki Bölgenin Stratigrafisi. *Süleyman Demirel Üniversitesi Fen Bilimleri Enstitüsü Dergisi*, *1*, 43–64.

Hunt, J. D., Nascimento, A., Guzman, O. J. R., Furtado, G. C. d. A., ten Caten, C. S., Tomé, F. M. C., Leal Filho, W., Durin, B., Lopes, M. & Wada, Y. (2022). Sedimentary basin water and energy storage: a low environmental impact option for the Bananal Basin. *Energies*, *15*, Article 4498. https://doi.org/10.3390/en15124498

Işık, M. & Şenel, H. (2009). 3D gravity modeling of Büyük Menderes basin in Western Anatolia using parabolic density function. *Journal of Asian Earth Sciences*, *34*(3), 317–325. https://doi.org/10.1016/j.jseaes.2008.05.013

Karaman, M. E., Meriç, E. & Tansel, İ. (1988). Çünür (Isparta) dolaylarında Kretase-Tersiyer geçişi. *Akdeniz Üniversitesi Isparta Mühendislik Fakültesi Dergisi, 4*, 80–100.

Kissel, C. & Poisson, A. (1986). Etude paléomagnétique préliminaire des formations néogènes du bassin d'Antalya (Taurides occidentales, Turquie). *Comptes Rendus de l'Académie des Sciences Paris*, *302*, 711–716.

Koçyiğit, A. & Özacar, A. (2003). Extensional neotectonic regime through the NE edge of the outer Isparta Angle, SW Turkey: new field and seismic data. *Turkish Journal of Earth Sciences*, *12*(1), 67–90.

Lima, W.A. & Silva, J.B. (2014). Combined modeling and smooth inversion of gravity data from a faulted basement relief. *Geophysics*, *79*(6), F1–F10. https://doi.org/10.1190/geo2013-0357.1

McKenzie, D.P. (1972). Active tectonics of the Mediterranean region. *Geophysical Journal International*, *30*(2), 109–185. https://doi.org/10.1111/j.1365-246X.1972.tb02351.x

Murthy, I. R. & Rao, S. J. (1989). A Fortran 77 program for inverting gravity anomalies of two-dimensional basement structures. *Computers & Geosciences, 15*(7), 1149-1156. https://doi.org/10.1016/0098-3004(89)90126-X

Okay, A.I. & Tüysüz, O. (1999). Tethyan sutures of northern Turkey, in The Mediterranean Basins: Tertiary extension within the Alpine Orogen. In Durand, B., Jolivet, L., Horvath, F. & Seranne, M.(Eds.), *Geological Society of London, Special Publications*, *156,* pp. 475–515.

Onajite, E. (2014). Understanding seismic interpretation methodology. In Seismic Data Analysis Techniques in Hydrocarbon Exploration, pp. 177–211, Elsevier. https://doi.org/10.1016/B978-0-12-420023-4.00013-7

Pamuk, E., Akgün, M., Özdağ, Ö. C. & Gönenç, T. (2017). 2D soil and engineering-seismic bedrock modeling of eastern part of Izmir inner bay/Turkey. *Journal of Applied Geophysics*, *137*, 104–117. https://doi.org/10.1016/j.jappgeo.2016.12.016

Piper, J. D. A., Gürsoy, H. & Tatar, O. (2002). Palaeomagnetic evidence for the Gondwanian origin of the Taurides and rotation of the Isparta Angle, southern Turkey. *Geological Journal*, *37*(4), 317–336. https://doi.org/10.1002/gj.920

Rao, B. S. R. & Murthy. I. V. R. (1978). *Gravity and magnetic methods of prospecting*: Arnold-Heinemann (India) Pvt. Ltd., AB, 9 Safdar jang Enclave. New Delhi, 390 p.

Rao, D. B., Prakash, M. J. & Babu, N. R. (1990). 3D and 2½ D modelling of gravity anomalies with variable density contrast. *Geophysical Prospecting*, *38*(4), 411–422. https://doi.org/10.1111/j.1365-2478.1990.tb01854.x

Reilinger, R., McClusky, S., Vernant, P., Lawrence, S., Ergintav, S., Cakmak, R. … & Karam, G. (2006). GPS constraints on continental deformation in the Africa–Arabia–Eurasia continental collision zone and implications for the dynamics of plate interactions. *Journal of Geophysical Research: Solid Earth*, *111*(B5), Article B05411. https://doi.org/10.1029/2005JB004051

Robertson, F., Poisson A. H. A. & Akinci, Ö. (2003). Developments in research concerning Mesozoic–Tertiary Tethys and neotectonics in the Isparta Angle, SW Turkey. *Geological Journal*, *38*(3-4), 195–234. https://doi.org/10.1002/gj.953

Roy, A., Ekinci, Y. L., Balkaya, Ç. & Ai, H. (2025). Deep learning-based inversion with discrete cosine transform discretization for two-dimensional basement relief imaging of sedimentary basins from observed gravity anomalies. *Geophysical Prospecting*, *73*(1), 113–129. https://doi.org/10.1111/1365-2478.13647

Sari, C. & Şalk, M. (2006). Sediment thicknesses of the western Anatolia graben structures determined by 2D and 3D analysis using gravity data. *Journal of Asian Earth Sciences*, *26*(1), 39–48. https://doi.org/10.1016/j.jseaes.2004.09.011

Seed, H. B. & Idriss, I. M. (1982). *Ground motions and soil liquefaction during earthquakes*. Earthquake Engineering Research Institute, Berkeley, California, 243 pp.

Silahtar, A., Kanbur, M. Z. & Beyhan, G. (2020). Investigation of a sedimentary basin by using gravity and seismic reflection data in the Isparta basin, southwestern Turkey. *Bulletin of Engineering Geology and the Environment*, *79*(8), 3971–3988. https://doi.org/10.1007/s10064-020-01804-z

Şenel, M. (2007a). *1:100.000 ölçekli Türkiye Jeoloji Haritası, Isparta M24 (J10)*. Maden Tetkik ve Arama Genel Müdürlüğü Yayını, Ankara.

Şenel, M. (2007b). 1*:100.000 ölçekli Türkiye Jeoloji Haritası, Isparta M25 (J11)*. Maden Tetkik ve Arama Genel Müdürlüğü Yayını, Ankara.

Şengör, A. M. C. & Yılmaz, Y. (1981). Tethyan evolution of Turkey: a plate tectonic approach. *Tectonophysics*, 75(3–4), 181–241. https://doi.org/10.1016/0040-1951(81)90275-4

Taymaz, T. & Price, S. (1992). The 1971 May 12 Burdur earthquake sequence, SW Turkey: a synthesis of seismological and geological observations. *Geophysical Journal International*, *108*(2), 589–603. https://doi.org/10.1111/j.1365-246X.1992.tb04638.x

Timur, E., Kaftan, I., Sari, C. & Şalk, M. (2019). Structure of the Büyük Menderes Graben systems from gravity anomalies. *Turkish Journal of Earth Sciences*, *28*(4), 544–557. https://doi.org/10.3906/yer-1809-31

Todd, D. K. & Mays, L. W. (2004). *Groundwater hydrology*, third edition. Wiley, New York, 656 pp.

Weissmann, G. S., Hartley, A. J., Scuderi, L. A., Nichols, G. J., Owen, A., Wright, S., Felicia A.L., Holland, F. & Anaya, F. M. L. (2015). Fluvial geomorphic elements in modern sedimentary basins and their potential preservation in the rock record: a review. *Geomorphology*, *250*, 187–219. https://doi.org/10.1016/j.geomorph.2015.09.005

Wessel, P. & Smith, W. H. (1995). New version of the generic mapping tools. *Eos, Transactions American Geophysical Union*, *76*(33), 329–329.

Wright, T. J., Parsons, B. E., Jackson, J. A., Haynes, M., Fielding, E. J., England, P. C. & Clarke, P. J. (1999). Source parameters of the 1 October 1995 Dinar (Turkey) earthquake from SAR interferometry and seismic bodywave modelling. *Earth and Planetary Science Letters*, *172*(1-2), 23–37. https://doi.org/10.1016/S0012-821X(99)00186-7

Wu, M., Liu, Z., Qin, Y., Su, K. & Yu, Z. (2025). Thermal property of reservoir rocks at thermal-mechanical coupled conditions and resultant impact on performance of geothermal systems. *Rock Mechanics and Rock Engineering*, *58*, 8773–8798. https://doi.org/10.1007/s00603-025-04587-5

Yalçınkaya, S. (1989). *Isparta-Ağlasun (Burdur) Dolaylarının Jeolojisi* [PhD Thesis]. İstanbul Üniversitesi.

Yıldız, A. & Toker, V. (1991). Çünür Köyü yöresindeki (Isparta kuzeyi) Üst Kretase-Eosen yaşlı birimlerin planktik foraminiferler ile biyostratigrafik incelemesi. *Türkiye Jeoloji Bülteni, 34*(2), 43–58. https://www.jmo.org.tr/resimler/ekler/5409b2c82d5925a_ek.pdf

Yiğitbaş, E., Elmas, A., Sefunç, A. & Özer, N. (2004). Major neotectonic features of eastern Marmara region, Turkey: development of the Adapazari–Karasu corridor and its tectonic significance. *Geological Journal, 39*, 179–198. https://doi.org/10.1002/gj.962